Robust Model Predictive Current Control for Dual-Star Induction Machine

Sofiane Brahami[1*], Kaci Ghedamsi[1], Abdelyazid Achour[2], Yanis Hamoudi[1]

[1] Université de Bejaia, Faculté de Technologie, Laboratoire de Maîtrise des Energies Renouvelables (LMER), 06000 Bejaia, Algeria
[2] Université de Bejaia, Faculté de Technologie, Laboratoire de Technologie Industrielle et de l'Information (LTII), 06000 Bejaia, Algeria
* Corresponding author, e-mail: sofiane.brahami@univ-bejaia.dz

Abstract

Predictive current control (PCC) is considered as an effective and efficient strategy for controlling multiphase drives, offering superior flexibility, fast dynamic response, and reduced computational complexity compared to conventional control methods. This paper presents a robust PCC approach for a dual-star induction machine (DSIM), integrated with direct field-oriented control (DFOC), using proportional-integral (PI) controllers to control mechanical speed and flux to analyze the efficiency of the drive system's behavior in complex challenging scenarios caused by motor's external perturbations and parameters uncertainties. The proposed PCC algorithm incorporates a two-step-ahead prediction horizon to evaluate a cost function that minimizes the deviation between reference and predicted stator currents. The control signal is selected from a finite set of voltage vectors (VVs) provided by a two-level voltage source inverter (2L-VSI), and the optimal switching states combination is selected to ensure precise control and improved performance. The proposed framework is validated through comprehensive simulations conducted in the Simulink/MATLAB environment. The findings achieved superior disturbances rejection capabilities, and minimized steady-state error. Furthermore, the system highlights an effective performance and robustness against simultaneous extreme parameters variations, especially under full load for very low speed scenario.

Keywords

model predictive current control, direct field-oriented control, dual-star induction motor, robustness

1 Introduction

Polyphase machines have attracted significant interest from researchers, manufacturers, and high power industrial applications due to their ability to mitigate the inherent limitations of traditional three-phase machines. By increasing the number of phases, these machines provide a more balanced distribution of power and current, thereby alleviating the limitations on switches and windings. Moreover, polyphase machines have numerous advantages not only minimize torque ripples but also reduce the peak amplitude of the generated torque, enhanced reliability, reduced rotor losses and improved efficiency, resulting in substantial improvements in dynamic performance [1, 2].

Classified as a six-phase induction machine (SPIM), the DSIM is one of the most widely used models, recognized for its cost-effectiveness and the additional degrees of freedom it offers. However, its nonlinear structure presents major challenge for control, making the decoupling of torque and flux essential for achieving independent

control. To ensure this, and also to achieve precision and control for speed and torque, advanced control techniques such as field-oriented control (FOC) and direct torque control (DTC) have been widely adopted [3]. DFOC has emerged as an effective approach. This advanced control technique enables variable speed functionality through the use of a power electronics inverter. DFOC allows the DSIM to be controlled in a manner similar to separately excited DC motors, offering regulation of both speed and flux using conventional PI controllers [4, 5].

Unfortunately, these control methods often struggle to deliver precise tuning of PI controllers, leading to performance degradation in the presence of external disturbances and parameter variations. As a result, the backstepping control (BSC) approach has been investigated in literature. Motivated by its success in three-phase induction motor applications [6, 7], the BSC has been extended and applied to DSIM [4, 8], demonstrating improved

tracking performance and disturbances rejection capabilities. Nevertheless, a notable disadvantage of this method remains in the complex gain adjustment process. In response to this challenge, sliding mode control (SMC) has gained attention. It is a nonlinear control technique that uses a discontinuous control law to drive the system dynamics to slide into a predetermined switching surface [9]. In [1] the SMC method was implemented on both a three-phase DSIM and a double open-winding induction motor (DOEWIM), with the aim of enhancing control precision and dynamic response across both topologies. In [10], a novel control scheme was proposed by combining indirect field-oriented control and third-order sliding mode control with the grey wolf optimization algorithm (IFOC-TOSMC-GWO) for DSIM, yielding notable improvements in overshoot reduction and robustness over parameter variations. Despite its advantages, its main drawback is the chattering phenomenon, caused by the high-frequency switching nature of the control law. Consequently, this leads to undesirable effects such as torque pulsations, current harmonics, and mechanical vibrations [11].

With the development in microprocessor technology, model predictive control (MPC) has evolved into a highly efficient and widely adopted control strategy for polyphase drive systems and power inverters. Unlike conventional techniques that require frequent tuning of PI controllers to address system uncertainties, MPC offers superior flexibility by allowing easy handling of nonlinear constraints such as significant internal and external disturbances [12, 13]. The continuous-set model predictive control (CS-MPC) faces challenges related to high computational demands and implementation complexity [14]. To overcome these issues, the finite-set model predictive control (FS-MPC) was introduced, leveraging the discrete nature of the converter's switching signals. FS-MPC operates by optimizing a cost function that calculates the deviation between the desired reference values and predicted future values at the next sampling time, the most optimized VV that achieves minimal errors is directly implemented to the inverter. This approach eliminates the need for modulation, simplifying the control process [15, 16]. A comparative study of FS-MPC and CS-MPC approaches for speed control of induction motor is implemented in [17].

Moreover, FS-MPC includes two main strategies: predictive torque control PTC and PCC, both designed to efficiently managing torque, flux, and motor speed. PTC directly regulates torque and flux, enabling faster torque response. The optimization process minimizes a cost

function defined by torque and flux errors. However, because this cost function involves these variables with distinct physical units, determining appropriate weighting factor can be complex and challenging, increasing system design difficulty. In contrast, PCC adopts an indirect approach by controlling the stator currents to influence torque and flux. This approach simplifies the control process through the elimination of weighting factor. By minimizing the error between reference and measured stator currents through an optimized cost function, PCC determines the optimal inverter switching states, ensuring accurate current tracking and effective motor control [18–23]. In [24], a multivariable generalized PTC was implemented for DSIM to minimize transient effects and mitigate measurement noise. Moreover, enhance performance especially under parameters variations in no-load condition.

Furthermore, an experimental study of PTC and PCC was implemented in [25, 26], highlighting that PCC excels in efficiency with reduced computational time, minimal tuning requirements, reduced current harmonic distortion, and enhanced resilience to stator resistance uncertainties. In contrast, PTC demonstrates superior performance in minimizing torque ripples and exhibits greater robustness against variations in magnetizing inductance. Despite these distinctions, both approaches achieve comparable and high-performance. PCC approach is more commonly used for SPIM providing a simplicity, reliability and a high performance control alternative against limitations associated with weighting factor design, variable switching frequency and high computation burden [27]. In [28, 29] PCC effect on current quality across different winding configurations layouts of SPIM, mainly double three-phase (D3P), asymmetrical (A6P) and symmetrical (S6P) was explored.

In [30, 31], a double d-q modeling approach was proposed as an alternative to the voltage space decomposition method. This strategy removes the requirement for weighting factor within the cost function, thereby simplifying the control system's design. In [32] modulated PCC was implemented to achieve a fixed switching frequency, enhancing steady-state performance and reducing x-y current components. A simplified PCC algorithm was proposed in [33], which effectively reduces the number of iterations needed during the optimization process.

A tailored PCC strategy for nine-switch inverter (NSI)-fed SPIM was implemented recently in [34], optimizing winding configurations D3P and A6P to reduce x-y currents and maximize α-β voltage, comparing it with FOC, and addressing post-fault performance under open converter

leg (OCL) conditions. However, as the complexity of the inverter rises, the number of possible VVs increase, leading to greater computational requirements, consequently contribute to larger current ripples, negatively impacting drive efficiency. Moreover, the requirement of fast digital processors can drive up costs, limiting industrial adoption if cost-effective implementation is not achievable [35, 36].

This paper proposes a robust PCC approach for a DSIM, integrated with DFOC, where rotor speed serves as the reference input variable. The algorithm incorporates a control law that optimizes a cost function by evaluating the errors between the measured and reference stator currents. Each stator set of the DSIM is powered by a 2L-VSI, renowned for its simplicity and reduced modulation requirements due to the limited number of semiconductor components. The 2L-VSI generates 2^3 which means 8 possible VVs, thereby reducing computational demands and cost. The primary contributions of the suggested approach are detailed in the following:

- Delivered a comprehensive evaluation of the system's dynamic performance, highlighting precise trajectory tracking and disturbances rejection while maintaining stability. This approach characterized for its simplicity, by eliminating the need for sophisticated design processes or weighting factor.
- Provided an in-depth analysis of the proposed approach, demonstrating its robustness and reliability against combined extreme parameters mismatches, particularly under full load conditions for both high and very low speed reference operations.

This paper is divided into several sections as follows: First, Section 2 represents the mathematical modeling of DSIM in the *d-q* referential frame. Section 3 elaborates the DFOC strategy for DSIM. While, Section 4 describes the 2L-VSI and the possible VVs it generates. Section 5 outlines the proposed of PCC algorithm applied for DSIM. Section 6 discusses the obtained simulation results and provides a technical comparative analysis between the proposed method and other approaches used in prior studies. Finally, conclusions are depicted in Section 7.

2 Mathematical modeling of the DSIM
The DSIM has two balanced three-phase stator windings: stator 1 and stator 2. The magnetic axes of the stators are separated by an electrical angle $\delta(\delta = 30°)$. The motor features a standard squirrel-cage rotor winding. Due to the distribution of its windings and its complex geometry, analyzing its exact configuration is challenging. Therefore, it is essential to adopt simplifying assumptions, such as assuming that the motor windings are distributed sinusoidally and neglecting magnetic circuit saturation. Both stators have identical parameters and feature a linear flux path [5]. In Fig. 1, the machine has two stator winding sets (a_{s1}, b_{s1}, c_{s1}) and (a_{s2}, b_{s2}, c_{s2}) shifted by δ, with isolated neutral points and a three-phase squirrel-cage rotor (a_r, b_r, c_r). θ is the angle shift between the rotor and star 1, and $(\theta - \delta)$ is the one between the rotor and star 2.

The electrical equations for modeling the DSIM in the *d-q* referential frame are [1, 37]:

$$
\begin{cases}
V_{ds1} = R_s i_{ds1} + \dfrac{d\Phi_{ds1}}{dt} + \omega_s \Phi_{qs1} \\[2mm]
V_{qs1} = R_s i_{qs1} + \dfrac{d\Phi_{qs1}}{dt} + \omega_s \Phi_{ds1} \\[2mm]
V_{ds2} = R_s i_{ds2} + \dfrac{d\Phi_{ds2}}{dt} + \omega_s \Phi_{qs2} \\[2mm]
V_{qs2} = R_s i_{qs2} + \dfrac{d\Phi_{qs2}}{dt} + \omega_s \Phi_{ds2} \\[2mm]
V_{dr} = 0 = R_r i_{dr} + \dfrac{d\Phi_{dr}}{dt} + (\omega_s + \omega_r)\Phi_{qr} \\[2mm]
V_{qr} = 0 = R_r i_{qr} + \dfrac{d\Phi_{qr}}{dt} + (\omega_s + \omega_r)\Phi_{dr}
\end{cases}
\tag{1}
$$

where, V_{ds1}, V_{qs1}, V_{ds2} and V_{qs2} are the *d-q* voltage components of the dual stator three-phase systems. i_{ds1}, i_{qs1}, i_{ds2} and i_{qs2} are the *d-q* stator current components of the dual stator systems. i_{dr} and i_{qr} are the *d-q* current components of the rotor. R_s, R_r are the stator and rotor resistances. ω_s is the speed of the synchronous reference frame, ω_r is the rotor
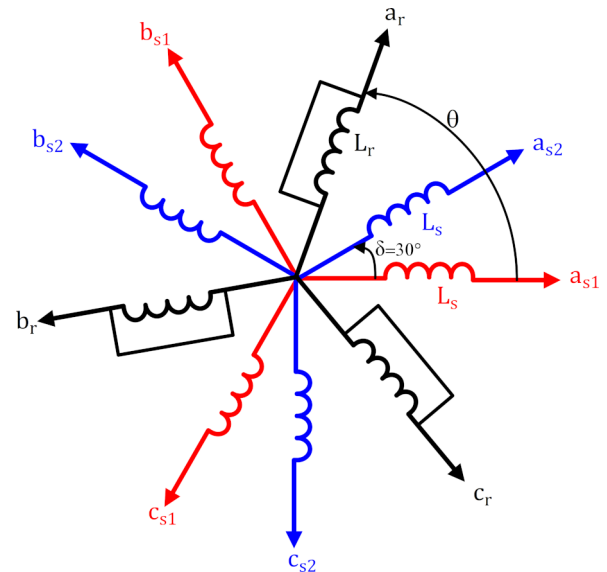

Fig. 1 Representation of DSIM windings in the *d-q* referential frame

electrical angular speed. The stator and rotor flux components Φ_{ds1}, Φ_{qs1}, Φ_{ds1}, Φ_{ds2}, Φ_{dr}, and Φ_{qr} are expressed by:

$$\begin{cases} \Phi_{ds1} = L_s i_{ds1} + L_m \left(i_{ds1} + i_{ds2} + i_{dr} \right) \\ \Phi_{qs1} = L_s i_{qs1} + L_m \left(i_{qs1} + i_{qs2} + i_{qr} \right) \\ \Phi_{ds2} = L_s i_{ds2} + L_m \left(i_{ds1} + i_{ds2} + i_{dr} \right) \\ \Phi_{qs2} = L_s i_{qs2} + L_m \left(i_{qs1} + i_{qs2} + i_{qr} \right) \\ \Phi_{dr} = L_r i_{dr} + L_m \left(i_{ds1} + i_{ds2} + i_{dr} \right) \\ \Phi_{qr} = L_r i_{qr} + L_m \left(i_{qs1} + i_{qs2} + i_{qr} \right) \end{cases}$$ (2)

where, L_s, L_r are the stator and rotor leakage inductances and L_m is the mutual inductance.

The electromagnetic torque is expressed by:

$$C_{em} = P \frac{L_m}{L_m + L_r} \left[\Phi_{dr} \left(i_{qs1} + i_{qs2} \right) - \Phi_{qr} \left(i_{ds1} + i_{ds2} \right) \right]$$ (3)

The mechanical dynamic equation is expressed by:

$$J \frac{d\Omega}{dt} = C_{em} - C_r - K_f \Omega,$$ (4)

where, P defines the number of pole pairs, J is the total moment of inertia, K_f denotes the viscous friction coefficient and C_r is the load torque.

Therefore, the model of DSIM in d-q subspace can be formulated as follows:

$$\begin{cases} \dot{x}(t) = Ax(t) + Bu(t) \\ y(t) = Cx(t) \end{cases}$$ (5)

With, $x(t) = [i_{ds1}\ i_{qs1}\ i_{ds2}\ i_{qs2}\ i_{dr}\ i_{qr}]^t$ expresses the state vector, $u(t) = [V_{ds1}\ V_{qs1}\ V_{ds2}\ V_{qs2}\ V_{dr}\ V_{qr}]^t$ the control input vector, and $y(t) = [i_{ds1}\ i_{qs1}\ i_{ds2}\ i_{qs2}\ i_{dr}\ i_{qr}]^t$ the output vector of the system.

With, $[A] = [L]^{-1}\{-\omega_{sl}[A_1] - [D]\}$, $[B] = [L]^{-1}[B_1]$ and $\omega_{sl} = (\omega_s - \omega_r)$ is the slip speed.

The matrices L, A_1, D, B_1, and C are defined by:

$$[L] = \begin{bmatrix} L_{1t} & 0 & L_m & 0 & L_m & 0 \\ 0 & L_{1t} & 0 & L_m & 0 & L_m \\ L_m & 0 & L_{2t} & 0 & L_m & 0 \\ 0 & L_m & 0 & L_{2t} & 0 & L_m \\ L_m & 0 & L_m & 0 & L_{rt} & 0 \\ 0 & L_m & 0 & L_m & 0 & L_{rt} \end{bmatrix}$$

$$[A_1] = \begin{bmatrix} 0 & 0 & 0 & 0 & 0 & 0 \\ 0 & 0 & 0 & 0 & 0 & 0 \\ 0 & 0 & 0 & 0 & 0 & 0 \\ 0 & 0 & 0 & 0 & 0 & 0 \\ 0 & -L_m & 0 & -L_m & 0 & -L_{rt} \\ L_m & 0 & L_m & 0 & -L_{rt} & 0 \end{bmatrix}$$

$$[D] = \begin{bmatrix} R_s & -D_1 & 0 & -D_m & 0 & -D_m \\ D_1 & R_s & D_m & 0 & D_m & 0 \\ 0 & -D_m & R_s & -D_2 & 0 & -D_m \\ \omega_s L_m & 0 & D_2 & R_s & D_m & 0 \\ 0 & 0 & 0 & 0 & R_r & 0 \\ 0 & 0 & 0 & 0 & 0 & R_r \end{bmatrix}$$

$$[B_1] = \begin{bmatrix} 1 & 0 & 0 & 0 & 0 & 0 \\ 0 & 1 & 0 & 0 & 0 & 0 \\ 0 & 0 & 1 & 0 & 0 & 0 \\ 0 & 0 & 0 & 1 & 0 & 0 \\ 0 & 0 & 0 & 0 & 0 & 0 \\ 0 & 0 & 0 & 0 & 0 & 0 \end{bmatrix}$$

$$[C] = \begin{bmatrix} 1 & 0 & 0 & 0 & 0 & 0 \\ 0 & 1 & 0 & 0 & 0 & 0 \\ 0 & 0 & 1 & 0 & 0 & 0 \\ 0 & 0 & 0 & 1 & 0 & 0 \\ 0 & 0 & 0 & 0 & 1 & 0 \\ 0 & 0 & 0 & 0 & 0 & 1 \end{bmatrix},$$

where, $L_{1t} = (L_s + L_m)$, $L_{2t} = (L_s + L_m)$, $L_{rt} = (L_r + L_m)$: are respectively the total inductance of stator 1, stator 2 and rotor.

Moreover, $D_1 = \omega_s L_{1t}$, $D_2 = \omega_s L_{2t}$ and $D_m = \omega_s L_{rt}$.

3 DFOC strategy for DSIM

In an ideal DFOC scenario, the rotor flux linkage axis is precisely aligned with the d-axis, enabling precise and independent control of both torque and flux, it follows that [38]:

$$\Phi_{dr} = \Phi^*$$ (6)

$$\Phi_{qr} = 0$$ (7)

By substituting Eqs. (6) and (7) into Eqs. (1) and (2), the following is given:

$$R_r i_{dr} + \frac{d\Phi^*}{dt} = 0 \quad \Rightarrow \quad i_{dr} = 0$$ (8)

$$R_r i_{qr} + \omega_{sl}^* \Phi^* = 0 \quad \Rightarrow \quad i_{qr} = -\frac{\omega_{sl}^* \Phi^*}{R_r}$$ (9)

The rotor currents in terms of the stator currents are derived from Eq. (2) as follows:

$$i_{dr} = \frac{1}{L_m + L_r} \left[\Phi^* - L_m \left(i_{ds1} + i_{ds2} \right) \right]$$ (10)

$$i_{qr} = -\frac{L_m}{L_m + L_r} \left(i_{qs1} + i_{qs2} \right)$$ (11)

Substituting Eqs. (10) and (11) into Eqs. (8) and (9), obtain:

$$\left(i^*_{ds1} + i^*_{ds2}\right) = \frac{\Phi^*}{L_m} \tag{12}$$

$$\omega^*_{sl} = \frac{R_r L_m}{\left(L_m + L_r\right)\Phi^*}\left(i_{qs1} + i_{qs2}\right) \tag{13}$$

Furthermore, the substitution of Eqs. (6) and (7) into Eq. (3), the electromagnetic torque is given by:

$$C^*_{em} = P\frac{L_m}{L_m + L_r}\Phi^*\left(i^*_{qs1} + i^*_{qs2}\right) \tag{14}$$

The two stator's windings are identical, so the powers provided by this two windings system are the same, hence: $i^*_{ds1} = i^*_{ds2}$ and $i^*_{qs1} = i^*_{qs2}$.

3.1 Determining of speed controller parameters

The speed control loop is a crucial component of this control system [37]. It manages the speed through an external loop, and the output of the regulator determines the reference electromagnetic torque C^*_{em}, as shown in Fig. 2.

The speed loop's PI controller transfer function is given by:

$$G_{pi}\left(s\right) = K_{ps} + \frac{K_{is}}{S}, \tag{15}$$

where, K_{ps}: is the proportional gain and K_{is}: is the integral gain, both are the parameters of the PI controller to be determined, and S is the Laplace operator.

The drive system's closed-loop transfer function is defined as:

$$\frac{\Omega}{\Omega^*} = \frac{K_{ps}S + K_{is}}{JS^2 + \left(K_f + K_{ps}\right)S + K_{is}} = \frac{1}{\tau_r S + 1} \tag{16}$$

By identification,

$$\begin{cases} K_{ps} = J/\tau_r \\ K_{is} = K_f/\tau_r \end{cases} \tag{17}$$

With the rotor electrical time constant of the system, $\tau_r = \frac{L_r + L_m}{R_r}$.

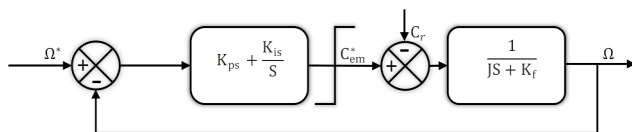The control must be limited by a saturation device defined by:

$$C^*_{em}\left(\text{lim}\right) = \begin{cases} C^*_{em} & \text{if } \left|C^*_{em}\right| \leq C^{\max}_{em} \\ C^{\max}_{em}\text{sign}\left(C^*_{em}\right) & \text{if } \left|C^*_{em}\right| \geq C^{\max}_{em} \end{cases}, \tag{18}$$

where, the maximum adopted torque for the DSIM is $C^{\max}_{em} = 40 \text{ Nm}$.

3.2 Rotor Flux estimation

By substituting Eq. (2) into Eq. (1), the rotor flux's components can be estimated by:

$$\begin{cases} \dfrac{d\Phi_{drest}}{dt} = \dfrac{R_r L_m}{L_r + L_m}\left(i_{ds1} + i_{ds2}\right) \\ -\dfrac{R_r}{L_r + L_m}\Phi_{drest} + \omega_{sl}\Phi_{qrest} \\ \dfrac{d\Phi_{qrest}}{dt} = \dfrac{R_r L_m}{L_r + L_m}\left(i_{qs1} + i_{qs2}\right) \\ -\dfrac{R_r}{L_r + L_m}\Phi_{qrest} - \omega_{sl}\Phi_{drest} \end{cases}, \tag{19}$$

where the rotor flux amplitude is given by:

$$\Phi_{rest} = \sqrt{\Phi^2_{drest} + \Phi^2_{qrest}} \tag{20}$$

3.3 Determining of the flux controller parameters

The diagram of the flux control loop is provided in Fig. 3, and its closed-loop transfer function is expressed as:

$$\frac{\Phi_{rest}}{\Phi^*} = \frac{2R_r L_m\left(K_{pf}S + K_{if}\right)}{\left(L_m + L_r\right)S^2 + \left(R_r + 2K_{pf}R_r L_m\right)S + 2K_{if}R_r L_m}$$
$$= \frac{1}{\tau_r S + 1} \tag{21}$$

By identification,

$$\begin{cases} K_{pf} = \left(L_r + L_m\right)/\left(2R_r L_m\tau_r\right) \\ K_{if} = 1/\left(2L_m\tau_r\right) \end{cases}. \tag{22}$$
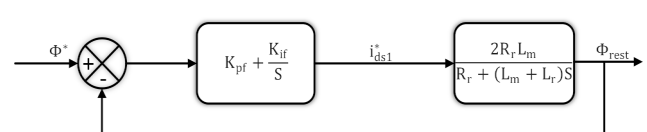

Fig. 2 Speed control loop

Fig. 3 Flux control loop

4 Inverter model

Each 2L-VSI independently supplies one of the dual stators winding sets of the DSIM, both connected to a shared DC bus constant voltage source. For high-power applications, semiconductor devices such as IGBTs or thyristors are used. The operating principle involves modulating the voltages applied to the stator windings through specific switching sequences. The generated voltages are determined by the states of the power converters legs, denoted as S_{ij}, where $i = a, b, c$ and $j = 1, 2$. $S_{ij} = 1$ identifies that the upper switch is activated and the lower switch is disabled, while $S_{ij} = 0$ means the opposite case. The switches operate in bipolar mode, with control signals directing the inverter output, as shown in Fig. 4 [39]. The voltages supplied to the first set of windings of the DSIM are expressed as:

$$\begin{bmatrix} V_{as1} \\ V_{bs1} \\ V_{cs1} \end{bmatrix} = \frac{V_{dc}}{3} \begin{bmatrix} 2 & -1 & -1 \\ -1 & 2 & -1 \\ -1 & -1 & 2 \end{bmatrix} \begin{bmatrix} S_{as1} \\ S_{bs1} \\ S_{cs1} \end{bmatrix} \qquad (23)$$

Similarly, the voltages supplied the second set of windings are given by:

$$\begin{bmatrix} V_{as2} \\ V_{bs2} \\ V_{cs2} \end{bmatrix} = \frac{V_{dc}}{3} \begin{bmatrix} 2 & -1 & -1 \\ -1 & 2 & -1 \\ -1 & -1 & 2 \end{bmatrix} \begin{bmatrix} S_{as2} \\ S_{bs2} \\ S_{cs2} \end{bmatrix} \qquad (24)$$

The 2L-VSI has double switches per phase, resulting in eight possible switching states ($2^3 = 8$) as in Table 1 [16]. Although the switching combinations for both inverters are identical, but the phase shift ensures that the second star's VVs are appropriately displaced in time as shown in Fig. 5. Two switching states, $\{S_{as1,2}, S_{bs1,2}, S_{cs1,2}\} = \{0, 0, 0\}$
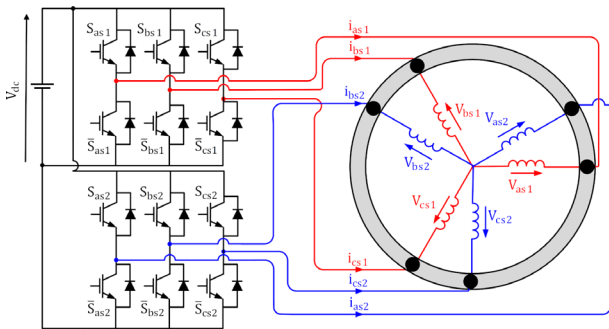
Fig. 4 The topology of the 2L-VSI

Table 1 The possible switching states for a 2L-VSI

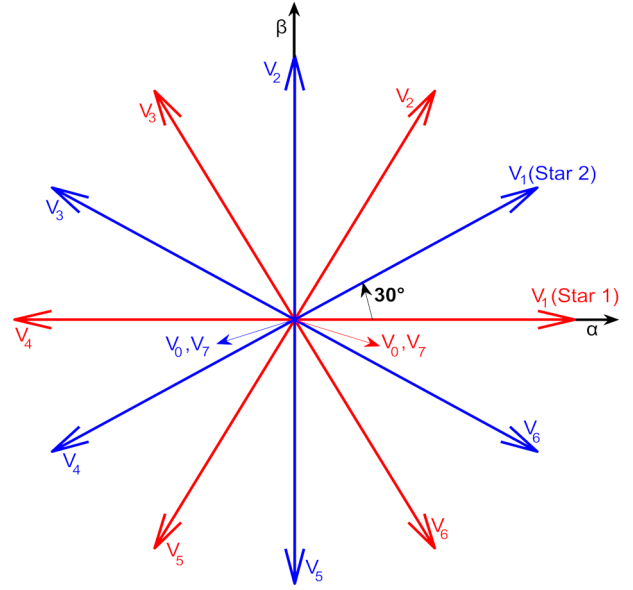|	V_0	V_1	V_2	V_3	V_4	V_5	V_6	V_7
$S_{as1,2}$	0	1	1	0	0	0	1	1
$S_{bs1,2}$	0	0	1	1	1	0	0	1
$S_{cs1,2}$	0	0	0	0	1	1	1	1

Fig. 5 Output space possible voltage vectors

and $\{S_{as1,2}, S_{bs1,2}, S_{cs1,2}\} = \{1, 1, 1\}$ are null VVs that effectively short-circuit the output, resulting zero voltage.

5 Proposed robust PCC application for DSIM

In this section, the structure of the suggested robust PCC approach for DSIM under DFOC is described , as shown in Fig. 6, where the superscript * represents the reference values. The control process begins with the measurement of stator currents and voltages, followed by the estimation of the machine's stator and rotor flux, both reference and measured values are rotated into the stationary α-β frame utilizing the inverse Park transformation and Clarke transformation. These flux estimations are then used by the algorithm model to predict the behavior of control variables over a two-step horizon ($k + 2$) for all possible switching states. The most appropriate optimized VV is then chosen by optimizing the cost function that aligns the predicted currents with the reference values, determining the switching state to be applied in the next sampling time.

The PCC algorithm is structured around three main stages: estimation, sub-space current prediction, and optimization of the cost function, which are outlined in these subsequent subsections [28, 29].
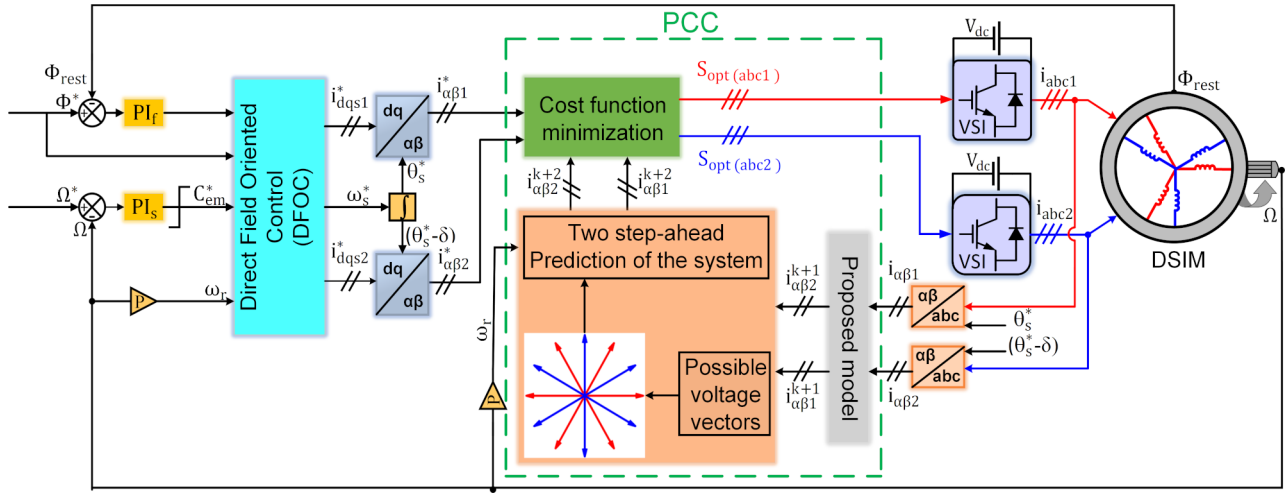
5.1 Estimation

The non-measured rotor and stator values are calculated using forward Euler discretization which can be described as follows:

$$\frac{dx}{dt} \approx \frac{x^{k+1} - x^k}{T_s}, \qquad (25)$$

where, T_s is the sampling time.

Fig. 6 General scheme of the proposed approach composed by an outer DFOC based speed and flux loops and an inner PCC loop for DSIM

In the stationary α-β frame where $\omega_s = 0$, the estimated stator and rotor fluxes can be obtained using Eqs. (1) and (2) from Eqs. (26) and (27) respectively, as follows:

$$\begin{cases} \Phi_{s1}^{k+1} = \Phi_{s1}^{k} + T_s v_{s1}^{k} - T_s R_s i_{s1}^{k} \\ \Phi_{s2}^{k+1} = \Phi_{s2}^{k} + T_s v_{s2}^{k} - T_s R_s i_{s2}^{k} \end{cases} \tag{26}$$

$$\Phi_{r\alpha\beta}^{k+1} = A \cdot \Phi_{s1,2}^{k+1} + B \cdot i_{s1,2}^{k}, \tag{27}$$

where, $A = \dfrac{L_r + L_m}{L_m}$ and $B = \dfrac{L_m^2 - (L_r + L_m)(L_s + L_m)}{L_m}$.

5.2 Prediction step

The one step ahead α-β currents are predicted based on stator and rotor corresponding dynamic equations by using the estimation step provided by Eqs. (26) and (27) and the measured stator voltage and current as defined by:

$$\begin{cases} i_{s1}^{k+1} = \left(1 - \dfrac{T_s}{\tau_\sigma}\right) i_{s1}^{k} \\ \quad + \dfrac{T_s}{R_\sigma (\tau_\sigma + T_s)} \left[k_r \left(\dfrac{1}{\tau_r} + j\omega_r\right) \Phi_r^{k} + v_{s1}^{k} \right], \\ i_{s2}^{k+1} = \left(1 - \dfrac{T_s}{\tau_\sigma}\right) i_{s2}^{k} \\ \quad + \dfrac{T_s}{R_\sigma (\tau_\sigma + T_s)} \left[k_r \left(\dfrac{1}{\tau_r} + j\omega_r\right) \Phi_r^{k} + v_{s2}^{k} \right] \end{cases} \tag{28}$$

where, $R_\sigma = R_s + R_r k_r^2$, $\tau_\sigma = \dfrac{\sigma (L_s + L_m)}{R_\sigma}$, $k_r = \dfrac{L_m}{L_r + L_m}$ and $\sigma = 1 - \left(\dfrac{L_m^2}{(L_s + L_m) L_r}\right)$.

The two step-ahead $(k + 2)$ prediction is defined by considering the computational delay caused by the controller, as follows [15]:

$$\begin{cases} i_{s1}^{k+2} = \left(1 - \dfrac{T_s}{\tau_\sigma}\right) i_{s1}^{k+1} \\ \quad + \dfrac{T_s}{R_\sigma (\tau_\sigma + T_s)} \left[k_r \left(\dfrac{1}{\tau_r} + j\omega_r\right) \Phi_r^{k+1} + v_{s1}^{k+1} \right] \\ i_{s2}^{k+2} = \left(1 - \dfrac{T_s}{\tau_\sigma}\right) i_{s2}^{k+1} \\ \quad + \dfrac{T_s}{R_\sigma (\tau_\sigma + T_s)} \left[k_r \left(\dfrac{1}{\tau_r} + j\omega_r\right) \Phi_r^{k+1} + v_{s2}^{k+1} \right] \end{cases} \tag{29}$$

5.3 Optimization step

Lastly, the optimization process involves selecting the optimal VV from the predefined subset of possible VVs. The control algorithm evaluates each vector using the cost function defined in Eqs. (30) and (31) and determines the one that minimizes this function, ensuring the best possible control action.

$$g_1 = \left(i_{\alpha1}^{*} - i_{\alpha1}^{k+2}\right)^2 + \left(i_{\beta1}^{*} - i_{\beta1}^{k+2}\right)^2 \tag{30}$$

$$g_2 = \left(i_{\alpha2}^{*} - i_{\alpha2}^{k+2}\right)^2 + \left(i_{\beta2}^{*} - i_{\beta2}^{k+2}\right)^2 \tag{31}$$

where, $i_{\alpha\beta1}^{*}$ and $i_{\alpha\beta2}^{*}$ are the α-β reference values derived from the specified torque and flux references.

With: $V_{Sopt1,2} = \arg\min\left\{ g_{1,2}\left(V_{1,2}^{k+1}\right) \big| \{V_0, \dots, V_7\} \right\}$.

6 Simulation results

To evaluate the effectiveness of the proposed PCC strategy, a comprehensive simulation study was carried out in the Simulink/MATLAB environment [40]. The DSIM's parameters used are provided in Table A1 in the Appendix. A sampling time of $T_s = 10$ µs was chosen to ensure adequate resolution and accuracy in capturing system's dynamic behavior under various challenging scenarios. Moreover, the suitability and efficiency of the proposed robust PPC are evaluated in contrast to the previous control approaches applied for DSIM.

6.1 Tracking performance and disturbance rejection

For the first set, while operating under fixed parameters, the system is tested under reference speed of $\Omega^* = 300$ rad/s, which is reversed to −300 rad/s at $t = 3.5$ s. Starting at $t = 1.5$ s, a nominal load torque of 14 N.m is introduced, the flux amplitude is kept constant at 1 Wb.

Fig. 7 illustrates that the speed promptly reaches the reference value at $t = 0.53$ s. When the load torque is introduced at $t = 1.5$ s, the speed experiences a minor drop but quickly recovers to the desired target after 0.005 s, demonstrating the PCC algorithm's effectiveness in rejecting disturbances and ensuring rapid convergence to the desired value. At $t = 3.5$ s, the control strategy achieves a quick deceleration for the speed reversal tracking, reaching −300 rad/s by $t = 4.19$ s, highlighting the system's dynamic response. Figs. 8 and 9 show the DSIM's electromagnetic torque which initially reaches a peak value of 39.3 N.m and achieves steady-state at $t = 0.53$ s, settling to zero as the motor operates without load. Starting from $t = 1.5$ s the motor's output torque increases to accommodate the applied load. Upon the reversal of speed,
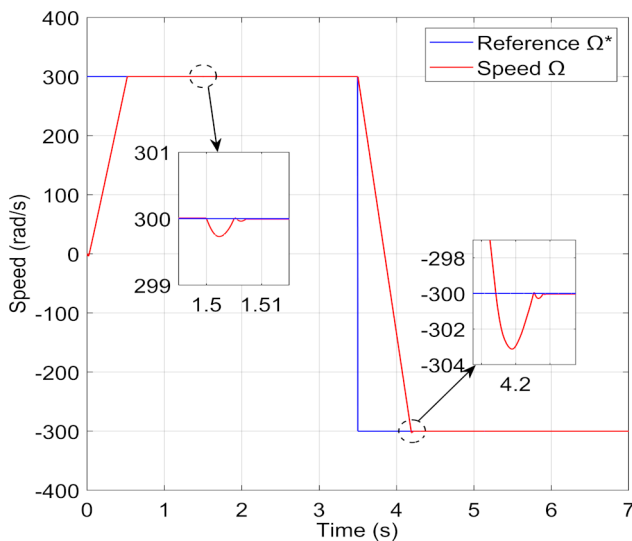

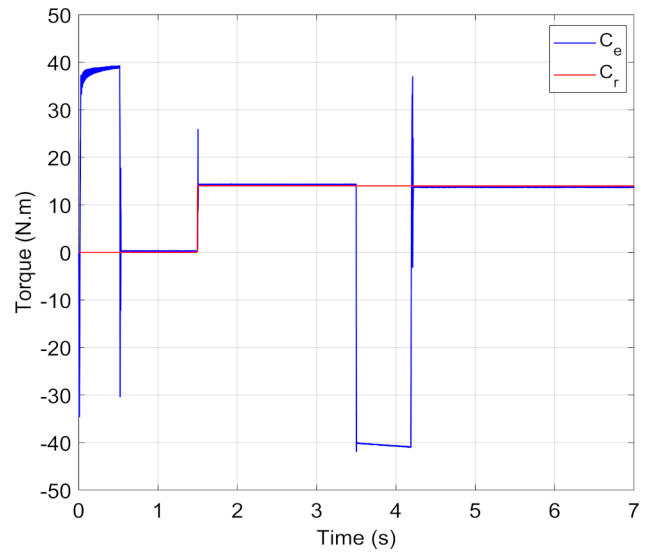**Fig. 7** Speed trajectory tracking response under load condition

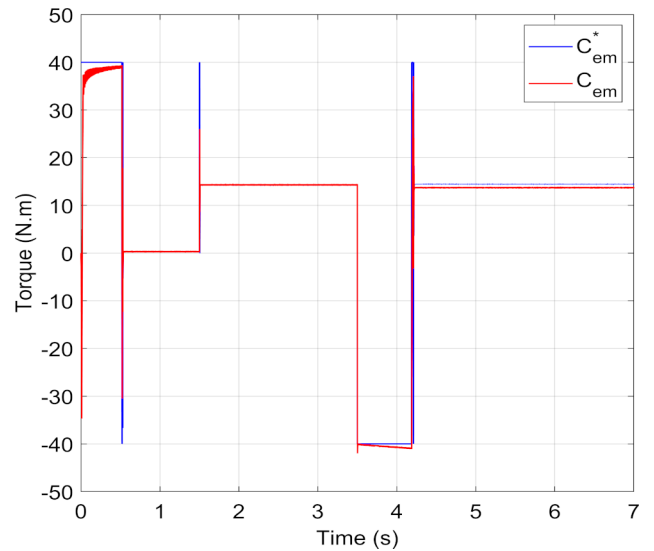**Fig. 8** Electromagnetic and load torque

Fig. 9 Tracking response of the electromagnetic torque

the torque reaches its maximum and then adjusts to match the estimated load torque at $t = 4.19$ s, confirming the controller's capability to handle dynamic changes effectively.

Fig. 10 presents the stator currents, which reach a peak value of 16.5 A during transient state. The currents increase during load application and speed reversal, reaching magnitudes similar to those observed during start-up phase, while ensuring a high-quality sinusoidal waveform. Fig. 11 demonstrates that the rotor flux's direct-axis Φ_{dr} accurately tracks the target value of 1 Wb throughout the process, effectively rejecting perturbations. The quadrature-axis rotor flux component Φ_{qr} remains null, confirming the accurate orientation and decoupling provided by the DFOC.

Fig. 12 depicts the tracking speed error of the suggested control strategy which converges to zero over time,
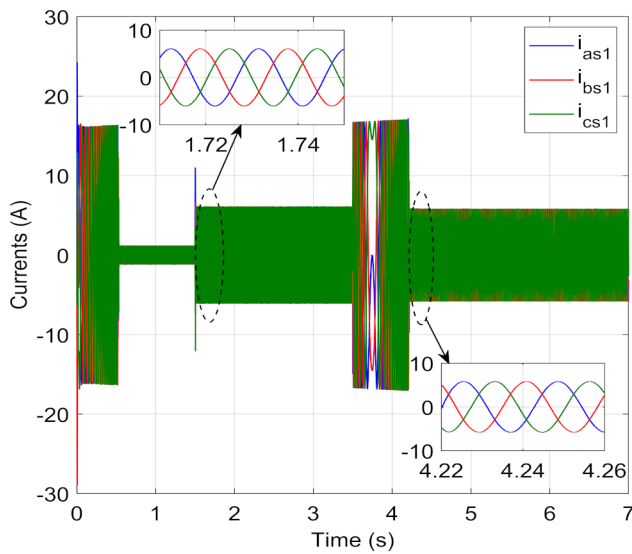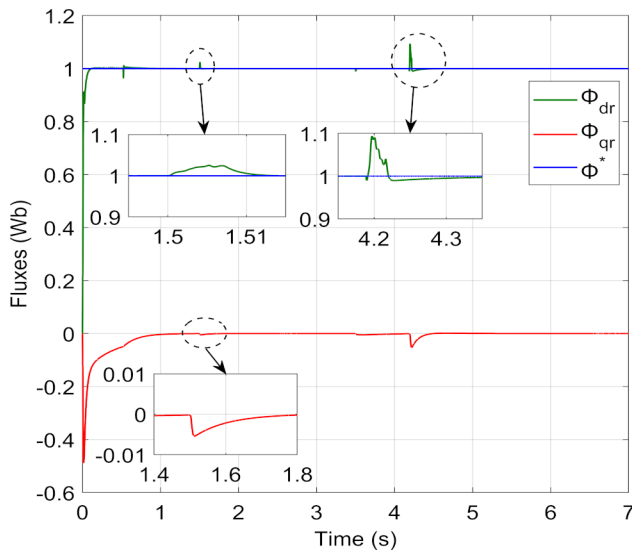
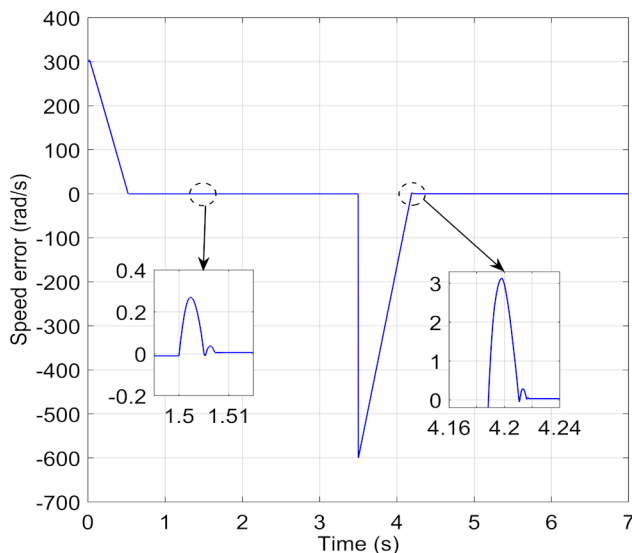**Fig. 10** Stator currents

Fig. 11 Fluxes norms

Fig. 12 Speed error response

the system exhibits an overshoot of 0.0032 rad/s in no-load condition and an overshoot of less than 0.006 rad/s from $t = 1.5$ s.

Table 2 shows the quantitative resume of PPC's performance under nominal external disturbance and speed reversal test. The modest overshoot of 0.03 rad/s observed during reversal operation is a consequence of the abrupt change in rotational direction, which generates transient electromagnetic fluctuations, resulting in a slight increase in electromagnetic torque, stator current, and rotor flux ripples values to 0.32 N.m, 0.13 A, and 0.00012 Wb, respectively.
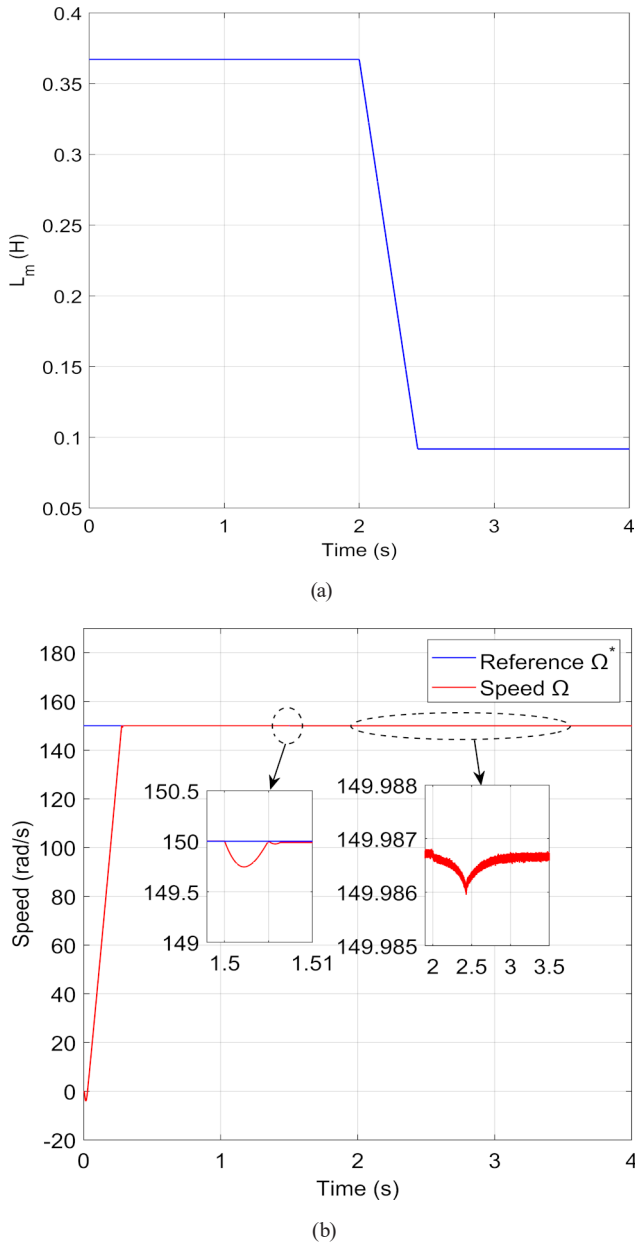
6.2 Robustness test

In this section, considering that the parameters of the DSIM are often linked to the machine's operating conditions (such as heating, load variations, magnetic circuit saturation, skin effect, etc.), it is crucial to evaluate the system's drive robustness under extreme significant electrical and mechanical parameters variations from their nominal values: 75% reduction in mutual inductance ($L_m = 0.0918$ H), 150% increase in stator resistance ($R_s = 9.3$ Ω) and augmenting the total inertia moment by 100 times ($J = 6.25$ kg.m^2). The system is simulated under $\Omega^* = 150$ rad/s with both individual and simultaneous parameters variations. Moreover, combined parameters variations are tested under $\Omega^* = 10$ rad/s for a very low speed scenario. All tests are conducted at full load torque of 14 N.m introduced starting at $t = 1.5$ s. Variations in parameters were implemented progressively with a slope of 60° starting at $t = 2$ s. Fig. 13(a) illustrates a 75% reduction in mutual inductance from the nominal value.

Fig. 13(b) shows the rotor speed tracks the target value of 150 rad/s, a slight dip was observed at $t = 1.5$ s due to 14 N.m load torque application. At $t = 2$ s, the rotor speed experiences a minor drop due to parameter variation but stabilizes near the reference with a small overshoot of 0.023 rad/s. Fig. 14 shows that at $t = 1.5$ s, fluxes norms experience a transient due to the applied load torque but recover quickly. Following the 75% reduction in L_m, Φ_{dr} drops slightly with minimal overshoot before stabilizing, while Φ_{qr} deviates persistently from zero, indicating slight flux decoupling deterioration. This demonstrates minor

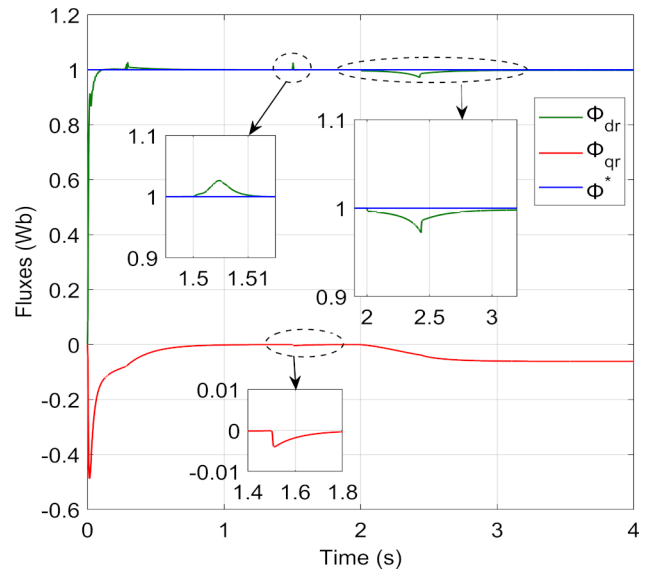**Table 2** Quantitative resume of PCC's performance under nominal disturbance and speed reversal

C_r (N.m)	Ω^* (rad/s)	Overshoot (rad/s)	Torque ripples (N.m)	Current ripples (A)	Flux ripples (Wb)
14	300	0.006	0.29	0.08	0.00011
14	−300	0.03	0.32	0.13	0.00012

(a)

Fig. 14 Fluxes norms results of -75% L_m under $\Omega^* = 150$ rad/s

(b)
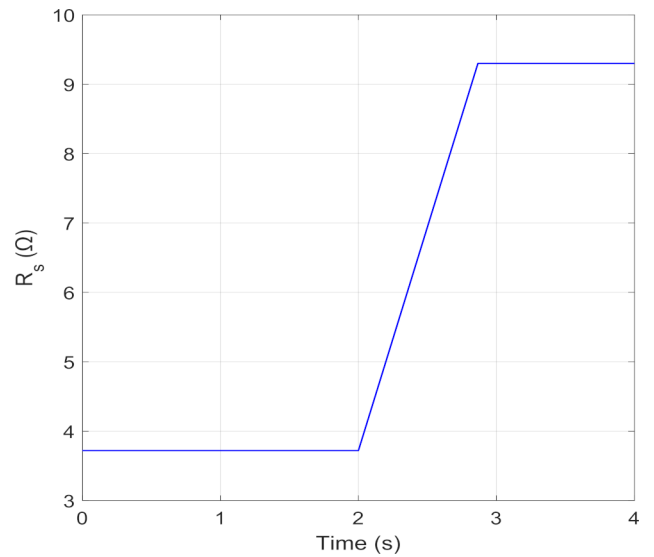

Fig. 15 Signal variation of $+150\%$ R_s

Fig. 13 Simulation results of reducing the mutual inductance by 75% from the nominal value under $\Omega^* = 150$ rad/s, (a) signal variation of -75% L_m, (b) speed trajectory tracking

PCC's sensitivity to severe L_m variation, typically caused by magnetic saturation, which also affects the reference currents, degrading control accuracy.

Fig. 15 shows the increase of R_s by 2.5 times from the nominal value. This increase typically caused by winding temperature variations, results in a negligible speed reduction with insignificant impact on the performance, as depicted in Fig. 16(a). Similarly, Fig. 17(a) illustrates the increase of J by 100 times from the nominal value, leading to unaffected speed with reduced oscillations, as shown in Fig. 17(b). The flux norms in Fig. 16(b) and Fig. 17(c) also

demonstrate insensitivity to these variations, despite the drop at $t = 1.5$ s due to the load torque application. These observations highlight the system's exceptional stability despite severe variations in R_s and J.

Fig. 18(a) illustrates the speed trajectory tracking under combined parameters variations under $\Omega^* = 150$ rad/s. At $t = 1.5$ s, the nominal torque application introduces a transient response, but the system recovers to accurately track the desired speed value. Following the parameters variations introduced at $t = 2$ s, the speed exhibits a slight overshoot but successfully rejects the perturbations and recovers gradually over time. The corresponding electromagnetic torque in Fig. 19(a) exhibits a steady behavior, where the measured torque closely tracks the applied
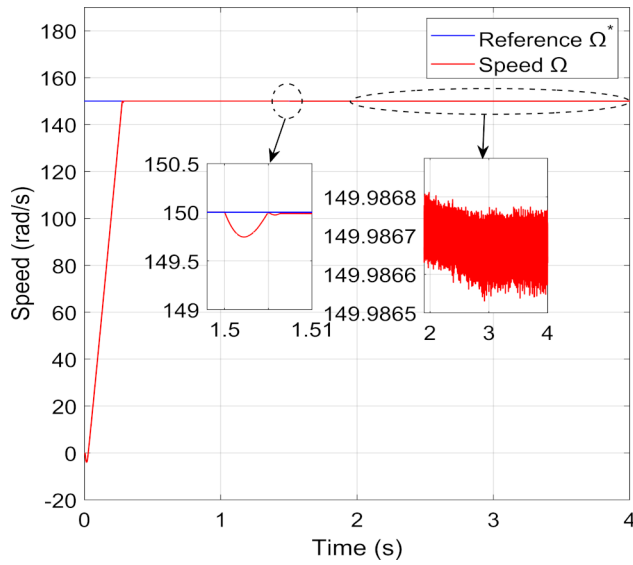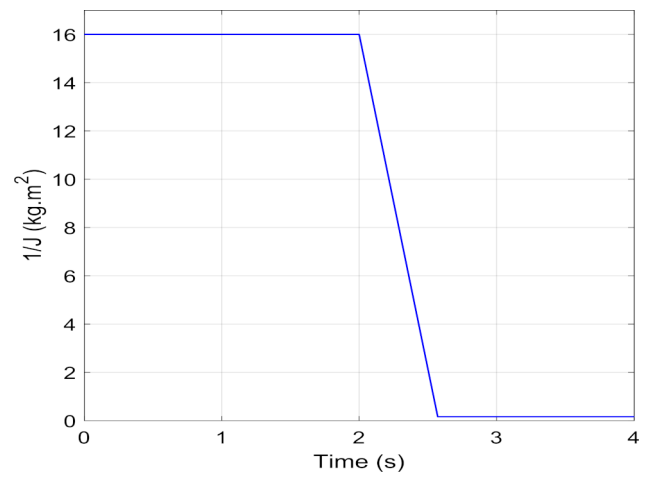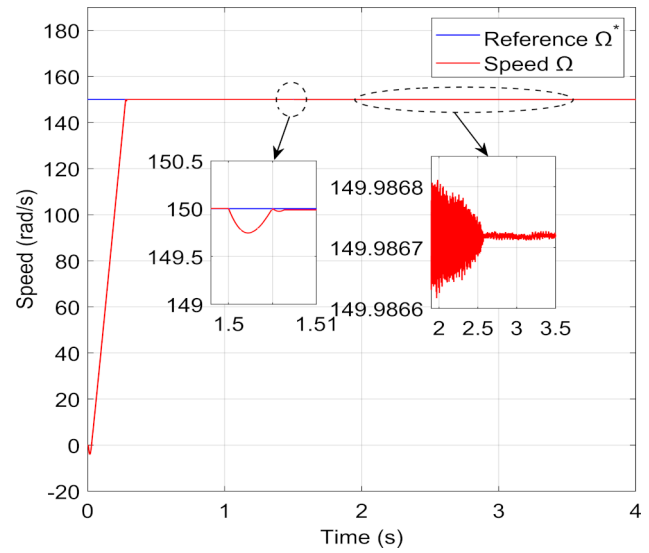
(a)
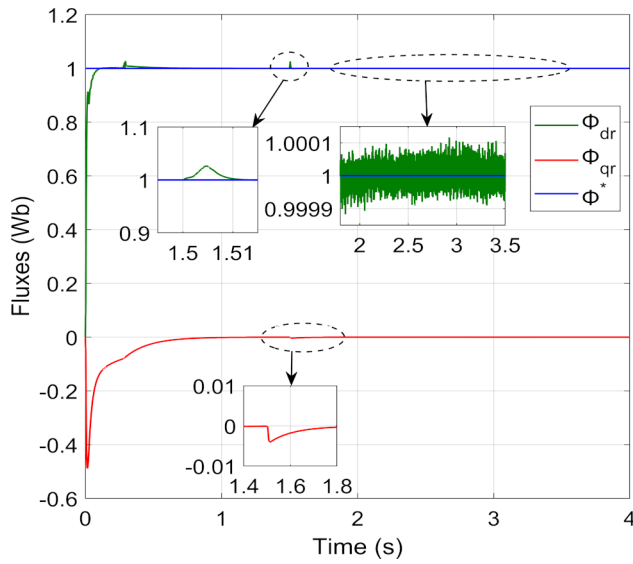
(b)

Fig. 16 Simulation results of increasing the stator resistance by 150% from the nominal value under $\Omega^* = 150$ rad/s, (a) speed trajectory tracking, (b) fluxes norms

load torque. In Fig. 20, for the very low speed scenario a slightly higher sensitivity is observed to the parameters variations, resulting in a marginally greater impact on the overshoot. Nevertheless, as shown in Fig. 21(b), the electromagnetic torque remains stable and the minimal ripples identified highlights the PCC's efficient capability to effectively overcome the applied perturbations. Fig. 18(b) and Fig. 21(a) depict the speed tracking errors under the influence of both the torque application and parameters variations. The errors converge toward zero over time, with final values of approximately 0.014 rad/s for the first test and 0.017 rad/s for the second one. These results demonstrate the PCC's robustness and the capacity to reject perturbations
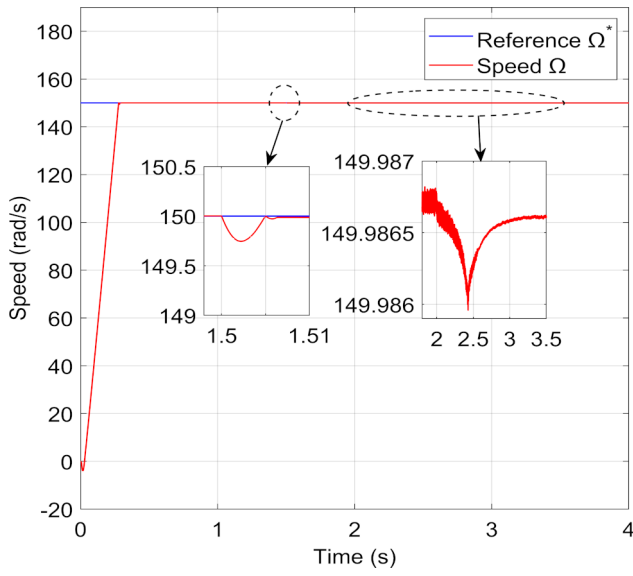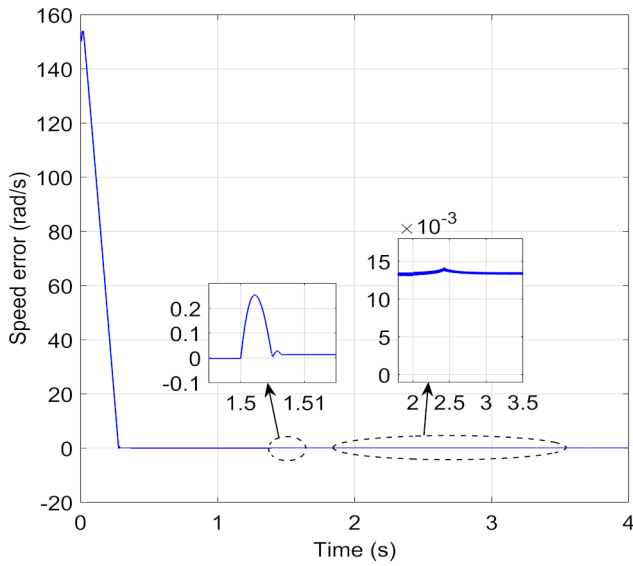

(a)

(b)
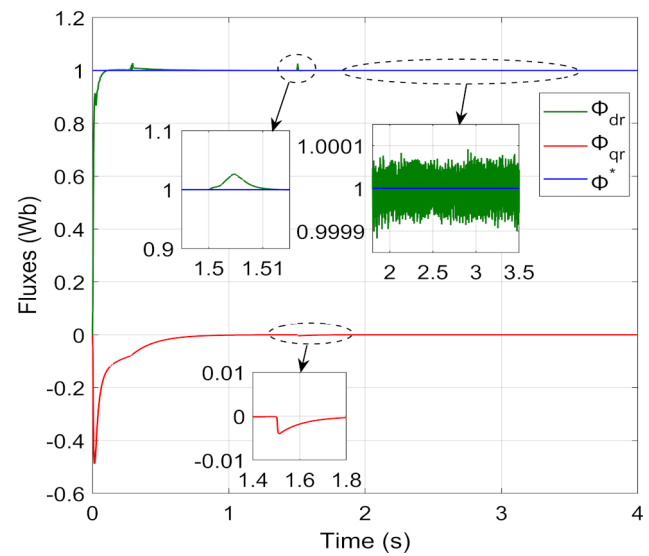
(c)

Fig. 17 Simulation results of increasing the total inertia moment 100 times from the nominal value under $\Omega^* = 150$ rad/s, (a) signal variation of + 100 times J, (b) speed trajectory tracking, (c) fluxes norms
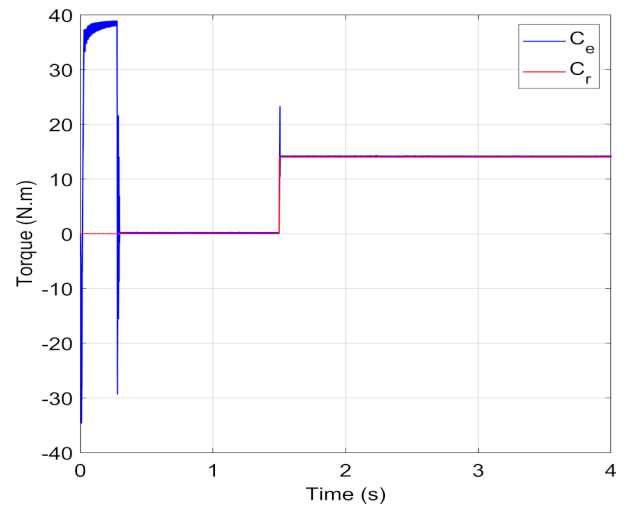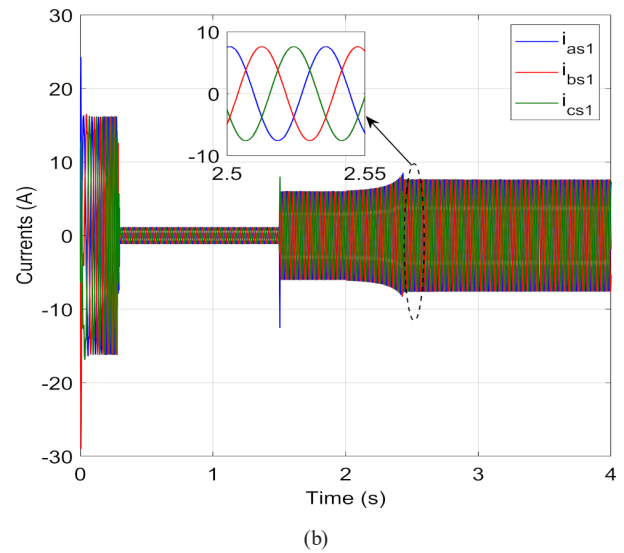
(a)

(b)

Fig. 18 Simulation results of combined variations, $-75\%\ L_m$, $+150\%\ R_s$ and $+100$ times J under $\Omega^* = 150$ rad/s, (a) speed response tracking, (b) speed error

effectively and ensure precise speed tracking even under the compounded effects of load application and significant parameters variations. The stator currents in Fig. 19(b) and Fig. 21(c), in both scenarios evolve in response to the application of load torque starting from $t = 1.5$ s. Then, the stator current exhibit a gradual increase in consumption due to the combined parameters variations of $-75\%\ L_m$, $+150\%\ R_s$ and $+100$ times J. Furthermore, the 120° phase difference between the currents is maintained throughout, ensuring stable and consistent waveform characteristics despite the perturbations. The fluxes norms in both Fig. 19(c) and Fig. 22 exhibit a transient response induced by the applied
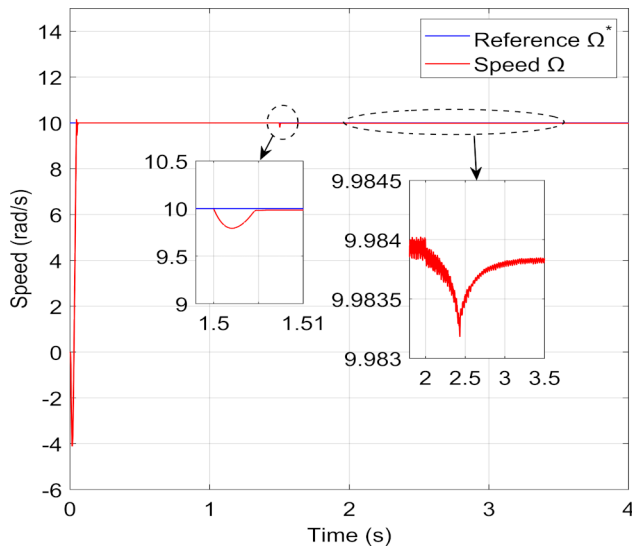

(a)

(b)
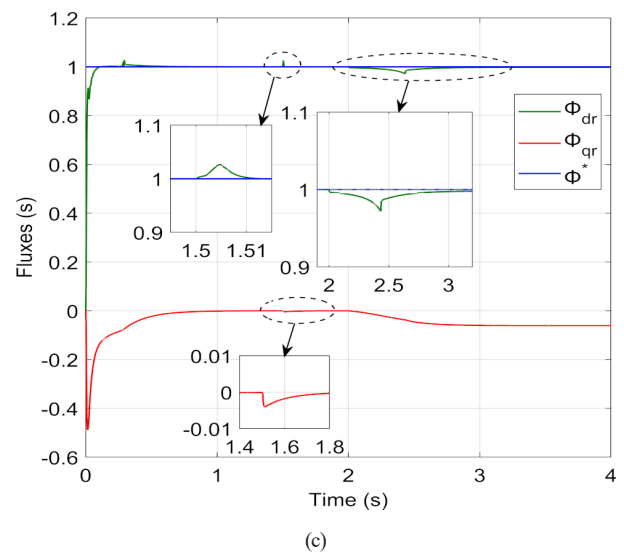
(c)

Fig. 19 Simulation results of combined variations, $-75\%\ L_m$, $+150\%\ R_s$ and $+100$ times J under $\Omega^* = 150$ rad/s, (a) electromagnetic and load torque, (b) stator currents, (c) fluxes norms
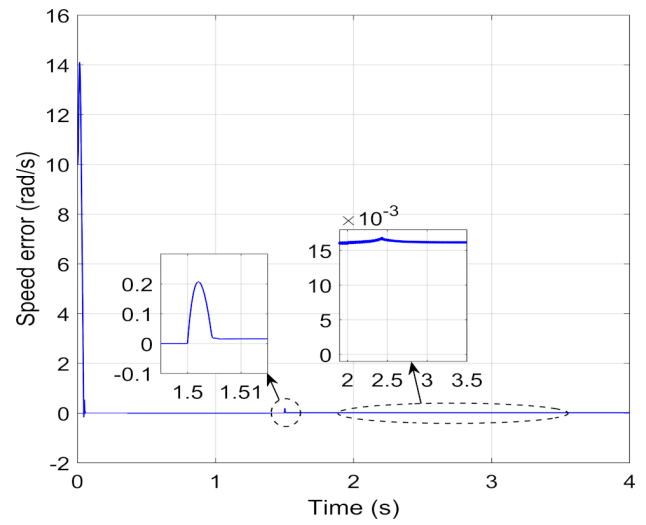
Fig. 20 Speed trajectory tracking under combined variations, −75% L_m, +150% R_s and +100 times J for a very low speed under $\Omega^* = 10$ rad/s

load torque and the subsequent combined parameters variations. Despite these perturbations, the flux norms gradually recover and stabilize at their reference values. However, the quadrature-axis rotor flux demonstrates a persistent slight deviation nearly −0.06 Wb, indicative of minor flux decoupling degradation attributed to the variation in L_m.
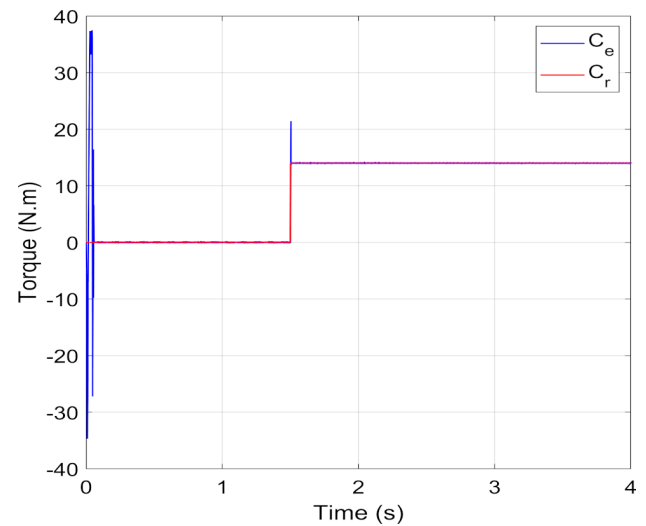
The effectiveness of the proposed method under extreme combined parameters uncertainties for wide range speed, which is the second objective of this study, is highlighted through an in-depth resume analysis presented in Tables 3 and 4. Furthermore, despite a slight increase particularly in current and flux ripples by 0.21 A and 0.00034 Wb, respectively which are observed for the very low speed tracking of 10 rad/s . The robust PCC guarantees powerful performance for various scenarios.

6.3 Comparative analysis

In this section, a comparative analysis is provided between the proposed method and recent approaches that have been investigated in the technical literature to improve DSIM's performance under challenging conditions, as summarized in Table 5. The conventional BSC strategy presented in [8] achieved a faster dynamic response compared to the traditional rotor field-oriented control (RFOC). However, this came at the expense of increased torque, current, and flux ripples, which negatively affected overall system stability and precision. In [4], an adaptive BSC integrated with an extended kalman filter (BSC-EKF) was proposed to enhance robustness by estimating speed, flux, and torque. While this approach improved adaptability to parameter uncertainties, it suffers from electromagnetic
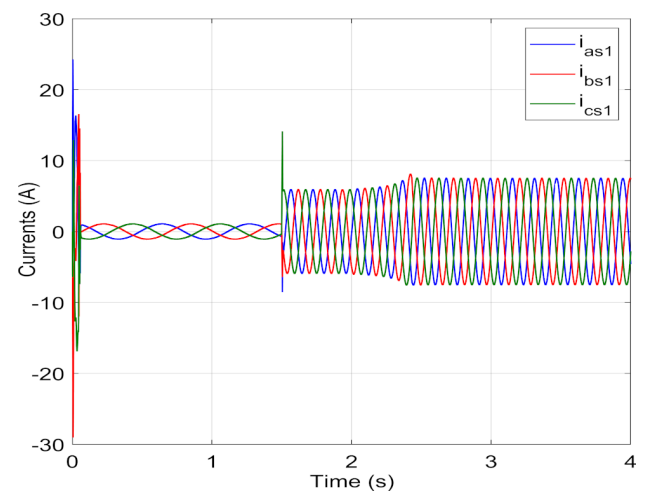
Fig. 21 Simulation results of combined variations, −75% L_m, +150% R_s and +100 times J for a very low speed scenario under $\Omega^* = 10$ rad/s, (a) speed error, (b) electromagnetic and load torque, (c) stator currents

Fig. 22 Fluxes norms under combined variations, −75% L_m, +150% R_s and +100 times J for a very low-speed scenario under $\Omega^* = 10$ rad/s
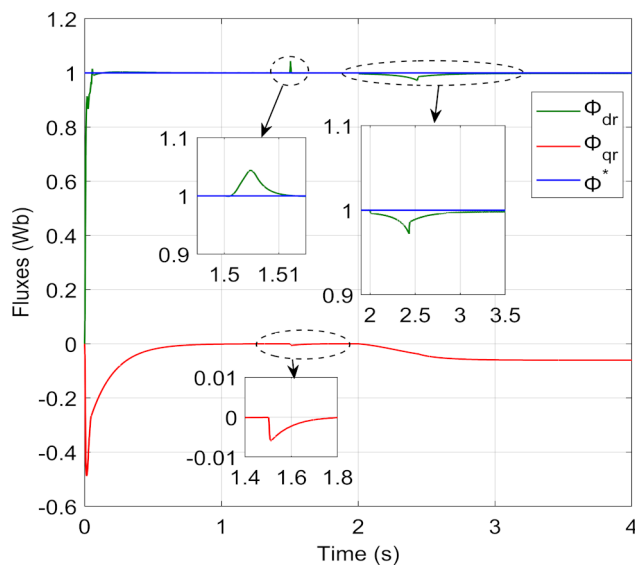
Table 3 Quantitative resume of PCC's performance under individual parameters uncertainties

Parameter variation	C_r (N.m)	Ω^* (rad/s)	Overshoot (rad/s)	Flux ripples (Wb)
−75% L_m	14	150	0.023	0.00014
+150% R_s	14	150	0.0133	0.00014
+100 times J	14	150	0.0133	0.00015

Table 4 Quantitative resume of PCC's performance under combined parameters uncertainties

Metric	Combined variations	Combined variations
Ω^* (rad/s)	150	10
C_r (N.m)	14	14
Overshoot (rad/s)	0.014	0.017
Torque ripples (N.m)	0.33	0.36
Current ripples (A)	0.13	0.21
Flux ripples (Wb)	0.00016	0.00034

torque fluctuations, current oscillations, and exhibited a high sensitivity to observer tuning. The novel hybrid IFOC-TOSMC-GWO strategy was introduced in [10] demonstrates superior tracking accuracy, robustness and ripples suppression compared to conventional IFOC-SMC technique. Nevertheless, its implementation remains computationally intensive, and the optimization algorithm requires complex tuning of numerous parameters.

In contrast, the robust PCC approach proposed in this study offers well-balanced advantages. It provides strong disturbance rejection and consistent performance across a broad speed range, including very low-speed operation, while handling severe variations in electrical and mechanical parameters. The PCC demonstrates better results compared to works presented in [4, 8, 10], without relying on complex design algorithm or weighting factor. This simplicity aligns with the main goal of the study. While its main limitation lies in sensitivity to system modeling, this can impact control accuracy and potentially lead to instability.

7 Conclusion

This paper investigates a comprehensive analysis of a robust PCC strategy application for a DSIM, highlighting a compelling alternative to conventional control methods due to its inherently simpler design. The approach leverages a two-step-ahead prediction algorithm to effectively overcome time delays. Optimal switching VVs for the 2L-VSI are determined by minimizing a cost function that accounts system constraints. Moreover, flux and electromagnetic torque decoupling are preserved through the integration of DFOC. Compared to previous control methods presented in [4, 8, 10], the proposed approach offers several advantages, ensures precise trajectory tracking, achieves a 60% improvement in disturbance rejection under nominal conditions and exhibits faster dynamic response. The robust

Table 5 A comparative analysis of the proposed method with previous approaches applied for DSIM

Publication reference	Approaches	Dynamic response (s)	Overshoot (rad/s)	Torque ripples (N.m)	Current ripples (A)	Flux ripples (Wb)	Sensitivity to external disturbances	Robustness	Model changes response
[8]	RFOC	0.42	High	High	High	High	High	Very low	Sensitive
[8]	BSC	0.17	Low	Medium	Medium	Medium	Low	Medium	Medium
[4]	BSC-EKF	0.33	Very low	Medium	Medium	Medium	Very Low	High	Sensitive
[10]	IFOC-SMC	0.226	0.4	2.99	1.2343	0.0126	Low	Medium	Medium
[10]	IFOC-TOSMC-GOW	0.2015	0.015	0.46	0.221	0.0025	Very low	High	Sensitive
Proposed	Robust PCC	0.195	0.006	0.29	0.08	0.00011	Robust	Robust	Sensitive

PCC significantly reduces ripples effect of electromagnetic torque, stator currents, and rotor flux by 36.95%, 63.8%, and 95.6%, respectively. Furthermore, the robustness of the demonstrated technique has been validated under severe simultaneous electrical and mechanical parameters mismatches, even -75% in L_m, $+150\%$ in R_s, and $+100$ times J. The strategy remains effective and demonstrates satisfactory performance across a wide range of mechanical speed reference, from high to very low at full load condition.

Future extensions of this study include experimental validation of the proposed method, integrating nonlinear controllers to overcome limitation of PI controllers to improve control flexibility, and examining the system's behavior under fault conditions.

References

[1] Sellah, M., Abdellah, K., Rezaoui, M. M. "Investigation of SVPWM Based Sliding Mode Control Application on Dual-Star Induction Motor and Dual Open-End Winding Induction Motor", Periodica Polytechnica Electrical Engineering and Computer Science, 66(1), pp. 80–98, 2022.
https://doi.org/10.3311/PPee.17910

[2] Moati, Y., Kouzi, K. "Investigating the Performances of Direct Torque and Flux Control for Dual Stator Induction Motor with Direct and Indirect Matrix Converter", Periodica Polytechnica Electrical Engineering and Computer Science, 64(1), pp. 97–105, 2020.
https://doi.org/10.3311/PPee.14977

[3] Ahmad, S., Le, H. T. "Effectiveness of Field Oriented Control and Direct Torque Control Methods for Induction Motor Speed Regulation", Wseas Transactions on Systems and Control, 18, pp. 531–526, 2023.
https://doi.org/10.37394/23203.2023.18.54

[4] Chaabane, H., Khodja, D. E., Chakroune, S., Hadji, D. "Model reference adaptive backstepping control of double star induction machine with extended Kalman sensorless control", Electrical Engineering & Electromechanics, 4, pp. 3–11, 2022.
https://doi.org/10.20998/2074-272X.2022.4.01

[5] Hellali, L., Belhamdi, S. "Speed control of doubly star induction motor (DSIM) using direct field oriented control (DFOC) based on fuzzy logic controller (FLC)", Advances in Modelling and Analysis C, 73(4), pp. 128–136, 2018.
https://doi.org/10.18280/ama_c.730402

[6] Zaafouri, A., Ben Regaya, C., Ben Azza, H., Chaari, A. "DSP-based adaptive backstepping using the tracking errors for high-performance sensorless speed control of induction motor drive", ISA Transactions, 60, pp. 333–347, 2016.
https://doi.org/10.1016/j.isatra.2015.11.021

[7] Ben Regaya, C., Ferhani, F., Zaafouri, A., Chaari, A. "A novel adaptive control method for induction motor based on Backstepping approach using dSpace DS 1104 control board", Mechanical Systems and Signal Processing, 100, pp. 466–481, 2018.
https://doi.org/10.1016/j.ymssp.2017.07.017

[8] Layadi, N., Zeghlache, S., Benslimane, T., Berrabah, F. "Comparative analysis between the rotor flux oriented control and backstepping control of a double star induction machine (DSIM) under open-phase fault", Advances in Modelling and Analysis C, 72(4), pp. 292–311, 2017.
https://doi.org/10.18280/ama_c.720407

[9] Quan, N. V., Long, M. T. "Sensorless sliding mode control method for a three-phase induction motor", Electrical Engineering, 104(5), pp. 3685–3695, 2022.
https://doi.org/10.1007/s00202-022-01578-5

[10] Terifa, E., Mendaci, S., Rezgui, S. E., Gasmi, H., Kantas, W. "Optimal third-order sliding mode controller for dual star induction motor based on grey wolf optimization algorithm", Heliyon, 10(12), e32669, 2024.
https://doi.org/10.1016/j.heliyon.2024.e32669

[11] Benderradji, H., Benaicha, S., Alaoui, L. C. "Improved sliding mode control for induction motor based on twisting algorithm", AIMS Electronics and Electrical Engineering, 9(1), pp. 81–98, 2025.
https://doi.org/10.3934/electreng.2025005

[12] Habib, A., Shawier, A., Mamdouh, M., Abdel-Khalik, A. S., Hamad, M. S., Ahmed, S. "Predictive current control based pseudo six-phase induction motor drive", Alexandria Engineering Journal, 61(5), pp. 3937–3948, 2022.
https://doi.org/10.1016/j.aej.2021.09.015

[13] Kasri, A., Ouari, K. "Robust Intelligent Nonlinear Predictive Control Based on Artificial Neural Network for Optimizing PMSM Drive Performance", Periodica Polytechnica Electrical Engineering and Computer Science, 68(4), pp. 356–366, 2024.
https://doi.org/10.3311/PPee.37217

[14] Varga, T., Benšić, T., Jerković Štil, V., Barukčić, M. "Continuous Control Set Predictive Current Control for Induction Machine", Applied Sciences, 11(13), 6230, 2021.
https://doi.org/10.3390/app11136230

[15] Hamoudi, Y., Amimeur, H., Nacef, S. "Finite-Set Model Predictive Power Control with Common Mode Voltage Elimination for an Asymmetrical Double-Star Induction Generator Wind Energy Conversion System", Majlesi Journal of Electrical Engineering, 17(3), pp. 125–136, 2023.
https://doi.org/10.30486/mjee.2023.1983159.1102

[16] Shahid, M. B., Jin, W., Abbasi, M. A., Li, L., Rasool, A., Bhatti, A. R., Sherefa Hussen, A. "Optimal weighting factor design based on entropy technique in finite control set model predictive torque control for electric drive applications", Scientific Reports, 14, 12791, 2024.
https://doi.org/10.1038/s41598-024-63694-5

[17] Ahmed, A. A., Koh, B. K., Lee, Y. I. "A Comparison of Finite Control Set and Continuous Control Set Model Predictive Control Schemes for Speed Control of Induction Motors", IEEE Transactions on Industrial Informatics, 14(4), pp. 1334–1346, 2018.
https://doi.org/10.1109/TII.2017.2758393

[18] Habibullah, M., Debanath, T., Shahadath Hossain Sabbir, M. "Fault Tolerant Control of Five-Phase Induction Motor Drive", In: El-Shahat, A. (ed.) Induction Motors - Recent Advances, New Perspectives and Applications, IntechOpen, 2023, pp. 95–112. ISBN 978-1-83769-578-2
https://doi.org/10.5772/intechopen.1001586

[19] Ma, S., Zhao, J., Xiong, Y., Ran, G., Yao, X. "Double-Closed-Loop Model Predictive Control Based on a Linear Induction Motor", Processes, 12(7), 1492, 2024.
https://doi.org/10.3390/pr12071492

[20] de Oliveira, L. M., Melo, V. F. M. B., da Paz, G. F., Rocha, F. V., Fabricio, E. L. L. "Experimental Assessment of Predictive Current Control Applied to Induction Machine Drive Systems Operating Under Single-Phase Open-Circuit Fault", Eletrônica de Potência, 29(1), pp. 1–12, 2024.
https://doi.org/10.18618/REP.2024.1.0011

[21] Ghalib, M. A., Hamad, S. A., Elmorshedy, M. F., Almakhles, D., Ali, H. H. "Beta Maximum Power Extraction Operation-Based Model Predictive Current Control for Linear Induction Motors", Journal of Sensor and Actuator Networks, 13(4), 37, 2024.
https://doi.org/10.3390/jsan13040037

[22] Xie, H., Wang, F., Chen, Q., He, Y., Rodrigez, J., Fellow, L., Kennel, R. "Computationally Efficient Predictive Current Control With Finite Set Extension Using Derivative Projection for IM Drives", IEEE Journal of Emerging and Selected Topics in Power Electronics, 11(2), pp. 1345–1357, 2023.
https://doi.org/10.1109/JESTPE.2022.3175904

[23] Taha, R. A., Abdel-Azim, W. E., Shawier, A., Metwly, M. Y., Abdel-Khalik, A. S., Hamad, M. S. "Single-Phase Charging of Six-Phase Integrated On-Board Battery Charger Using Predictive Current Control", IEEE Transactions on Transportation Electrification, 10(1), pp. 540–552, 2024.
https://doi.org/10.1109/TTE.2023.3289089

[24] Khouidmi, H., Massoum, A. "Predictive control based Speed, Torque and Flux Prediction of a Double Stator Induction Motor", Majlesi Journal of Electrical Engineering, 13(1), pp. 65–77, 2019. Available at: https://mjee.isfahan.iau.ir/article_696339.html [Accessed: 08 December 2024]

[25] Wang, F., Zhang, Z., Mei, X., Rodríguez, J., Kennel, R. "Advanced Control Strategies of Induction Machine: Field Oriented Control, Direct Torque Control and Model Predictive Control", Energies, 11(1), 120, 2018.
https://doi.org/10.3390/en11010120

[26] Wang, F., Li, S., Mei, X., Xie, W., Rodríguez, J., Kennel, R. "Model-Based Predictive Direct Control Strategies for Electrical Drives: An Experimental Evaluation of PTC and PCC Methods", IEEE Transactions on Industrial Informatics, 11(3), pp. 671–681, 2015.
https://doi.org/10.1109/TII.2015.2423154

[27] Mamdouh, M., Abido, M. A. "Current Gradient Based Modified Hysteresis Controller for Asymmetrical Six-Phase Induction Motor", IEEE Journal of Emerging and Selected Topics in Power Electronics, 12(5), pp. 5164–5175, 2024.
https://doi.org/10.1109/JESTPE.2024.3411715

[28] Shawier, A., Abdel-Majeed, M. S., Abdel-Azim, W. E., Abdel-Khalik, A. S., Hamad, M. S., Ahmed, S. "Effect of Winding Design on the Performance of Predictive Current Control of Six-Phase Induction Machine-Based Propulsion Systems", IEEE Access, 10, pp. 80587–80599, 2022.
https://doi.org/10.1109/ACCESS.2022.3194893

[29] Shawier, A., Habib, A., Mamdouh, M., Abdel-Khalik, A. S., Ahmed, K. H. "Assessment of Predictive Current Control of Six-Phase Induction Motor With Different Winding Configurations", IEEE Access, 9, pp. 81125–81138, 2021.
https://doi.org/10.1109/ACCESS.2021.3085083

[30] Mamdouh, M., Abdel-Khalik, A. S., Abido, M. A. "Predictive current control of asymmetrical six-phase induction motor without weighting factors", Alexandria Engineering Journal, 61(5), pp. 3793–3803, 2022.
https://doi.org/10.1016/j.aej.2021.09.003

[31] Mamdouh, M., Abido, M. A. "Weighting Factor Elimination for Predictive Current Control of Asymmetric Six Phase Induction Motor", In: 2020 IEEE International Conference on Environment and Electrical Engineering and 2020 IEEE Industrial and Commercial Power Systems Europe (EEEIC / I&CPS Europe), Madrid, Spain, 2020, pp. 1–6. ISBN 978-1-7281-7455-6
https://doi.org/10.1109/EEEIC/ICPSEurope49358.2020.9160671

[32] Ayala, M., Doval-Gandoy, J., Rodas, J., Gonzalez, O., Gregor, R., Rivera, M. "A Novel Modulated Model Predictive Control Applied to Six-Phase Induction Motor Drives", IEEE Transactions on Industrial Electronics, 68(5), pp. 3672–3682, 2021.
https://doi.org/10.1109/TIE.2020.2984425

[33] Mamdouh, M., Abido, M. A. "Simple Predictive Current Control of Asymmetrical Six-Phase Induction Motor With Improved Performance", IEEE Transactions on Industrial Electronics, 70(8), pp. 7580–7590, 2023.
https://doi.org/10.1109/TIE.2022.3217588

[34] Abdel-Moneim, M. G., Abdel-Azim, W. E., Abdel-Khalik, A. S., Hamed, M. S., Ahmed, S. "Model Predictive Current Control of Nine-Switch Inverter-Fed Six-Phase Induction Motor Drives Under Healthy and Fault Scenarios", IEEE Transactions on Transportation Electrification, 10(4), pp. 10125–10135, 2024.
https://doi.org/10.1109/TTE.2024.3368791

[35] Mamdouh, M., Salem, A., Abido, M. A. "Predictive Current Control for Three-level T-type Based Six-phase Induction Motor Drive", In: 2023 IEEE Power & Energy Society General Meeting (PESGM), Orlando, FL, USA, 2023, pp. 1–5. ISBN 978-1-6654-6441-3
https://doi.org/10.1109/PESGM52003.2023.10253262

[36] Serra, J., Jlassi, I., Cardoso, A. J. M. "A Computationally Efficient Model Predictive Control of Six-Phase Induction Machines Based on Deadbeat Control", Machines, 9(12), 306, 2021.
https://doi.org/10.3390/machines9120306

[37] Amimeur, H. "Contribution au Controle de la Machine Asynchrone Double Etoile" (Contribution to the Control of the Dual-Star Induction Machine), Doctorate in Sciences, Hadj Lakhdar University of Batna, 2012. Available at: http://eprints.univ-batna2.dz/id/eprint/1256 [Accessed: 08 December 2024] (in French)

[38] Bendjeddou, Y., Abdessemed, R., Merabet, E. "Improved field oriented control for stand alone dual star induction generator used in wind energy conversion", Engineering Review, 40(2), pp. 34–46, 2020.
https://doi.org/10.30765/er.40.2.05

[39] Nounou, K., Charpentier, J. F., Marouani, K., Benbouzid, M., Kheloui, A. "Fault-Tolerant Control of VSI Driven Double Star Induction Machine for Electric Naval Propulsion", In: 2018 IEEE International Power Electronics and Application Conference and Exposition (PEAC), Shenzhen, China, 2018.
https://doi.org/10.1109/PEAC.2018.8590291

[40] MathWorks, Inc. "MATLAB and SIMULINK, (R2020a)", [computer program] Available at: https://www.mathworks.com/products/matlab.html [Accessed: 01 September 2024]

Appendix

Table A1 DSIM parameters

Parameter	Value
P_n : Nominal power	4.5 kW
V_n : Nominal voltage	220 V
f : Frequency	50 Hz
N : Nominal Speed	3000 rpm
L_m : Mutual inductance	0.3672 H
L_r : Rotor leakage inductance	0.006 H
L_s : Stators leakage Inductance	0.022 H
R_s : Stators resistance	3.72 Ω
R_r : Rotor resistance	2.12 Ω
K_f : Viscous friction coefficient	0.001 N.m.s/rad
J : Total inertia moment	0.0625 kg.m^2
P : Number of pole pairs	1
V_{dc} : DC bus voltage	600 V